Exp. Theo. NANOTECHNOLOGY 10 (2026) 551-569 https://doi.org/10.56053/10.2.551

Tailoring the properties of alumina ceramic nanoparticles via chromium doping

Mojahid M. Najim[1], *Ban A. Yousif*[2], *Mohammed RASHEED*[3,*]

[1]Nanomaterials Research Center, University Of Anbar, Ramadi, Iraq
[2]Department of Applied Science, University of Technology- Iraq, Baghdad 10066, Iraq
[3]College of Production Engineering & Metallurgy, University of Technology- Iraq, Baghdad, Iraq
[*]) Email: rasheed.mohammed40@yahoo.com

Received 4/2/2026, *Received in revised form* 16/3/2026, *Accepted* 30/3/2026, *Published* 15/4/2026

Cr-doped Al_2O_3 (Al_2O_3:Cr) ceramic nanoparticles (AlCr0–AlCr5) are successfully synthesized via the sol–gel method and calcined at 1000 °C. X-ray diffraction (XRD) analysis confirmed the formation of a single-phase α-Al_2O_3 (corundum structure, space group R-3c) with characteristic reflections at 2θ ≈ 25.6°, 35.1°, 37.8°, 43.4°, 52.6°, and 57.5°. The crystallite size increased from ~25 nm for AlCr0 to ~36 nm for AlCr5, accompanied by a reduction in FWHM, indicating improved crystallinity with increasing Cr content. FTIR spectra exhibited characteristic Al–O vibrational bands in the 500–800 cm^{-1} region, while Raman analysis confirmed Eg and A1g modes of α-Al_2O_3 with enhanced peak intensity at higher doping levels. Density measurements showed an increase in bulk density from ~3.20 to ~3.35 g/cm^3 and a corresponding decrease in apparent porosity from ~28% to ~22% with increasing Cr concentration. Thermal analysis revealed total weight loss decreasing from ~6.0% (AlCr0) to ~4.3% (AlCr5), indicating enhanced thermal stability. DSC results showed an exothermic crystallization peak around ~800–830 °C, becoming sharper with Cr addition, while DTG confirmed reduced decomposition rates at higher doping levels. ICP-OES analysis demonstrated composition-dependent Cr^{3+} ion release, decreasing from ~0.007 ppm (AlCr0) to ~0.002 ppm (AlCr5), reflecting improved chemical stability. Cr incorporation enhances crystallinity, densification, thermal stability, and chemical resistance without altering the α-Al_2O_3 phase. Among all samples, AlCr5 exhibited the best overall performance, making it a promising candidate for advanced ceramic applications.

Keywords: Al_2O_3:Cr ceramic nanoparticles; Sol–gel; Structural; Thermal.

1. INTRODUCTION

Aluminum oxide (Al_2O_3), commonly known as alumina, is one of the most widely used ceramic materials due to its excellent mechanical strength, high thermal stability, chemical inertness, and good electrical insulation properties [1-4]. Among its various polymorphs, α-Al_2O_3 (corundum phase) is the most thermodynamically stable and technologically important form [5-7]. It is extensively utilized in applications such as catalysts, biomedical implants, coatings, sensors, and refractory materials [8-10]. With the advancement of nanotechnology, the development of Al_2O_3 in nanoparticle form has attracted significant attention, as reduced particle size enhances surface area and improves functional properties [11-15]. Doping Al_2O_3 with transition metal ions such as chromium (Cr^{3+}) has been widely investigated to tailor its structural, optical, and thermal properties [16-20]. Due to its similar ionic radius to Al^{3+}, Cr^{3+} can substitute into the alumina lattice without significantly disturbing the crystal structure [21,22]. This substitution can improve crystallinity, enhance grain growth, and modify electronic and optical behavior [23, 24]. Additionally, Cr doping is known to influence densification, reduce porosity, and improve thermal stability [25,26]. These effects make Cr-doped Al_2O_3 a promising material for advanced ceramic and optoelectronic applications [27,28]. Despite the advantages of Al_2O_3 ceramics, achieving high densification, improved crystallinity, and enhanced thermal stability at relatively moderate processing conditions remains a challenge [29,30]. Furthermore, controlling ion release and ensuring chemical stability are critical for applications in harsh environments and biomedical fields 31,32]. The influence of Cr doping concentration on these properties is not fully understood, particularly for sol–gel-derived Al_2O_3 nanoparticles processed at high temperatures [33-35]. Although several studies have reported the synthesis of doped alumina, there is limited systematic investigation on the combined effects of Cr doping on structural, thermal, and chemical properties, especially in terms of ion release behavior [36-40]. Moreover, correlations between crystallinity, densification, and thermal stability with varying Cr content are not comprehensively explored [41,42]. This motivates the present study to provide a detailed and comparative analysis of Cr-doped Al_2O_3 ceramic nanoparticles. The main objective of this work is to synthesize Cr-doped Al_2O_3 nanoparticles (AlCr0–AlCr5) using the sol–gel method and evaluate the effect of Cr concentration on their properties. The study focuses on structural characterization using XRD, FTIR, and Raman spectroscopy, thermal analysis using TGA, DSC, and DTG, and evaluation of physical properties such as density and porosity. Additionally, ICP-OES is employed to investigate Cr^{3+} ion release behavior, providing insight into chemical stability. This study provides a comprehensive investigation of Cr-doped Al_2O_3 ceramic nanoparticles, combining multiple characterization techniques to establish clear relationships between composition and material properties. The novelty lies in the systematic comparison of structural, thermal, and chemical stability, along with the inclusion of ion release analysis, which is rarely reported in similar studies. The work demonstrates how Cr doping enhances crystallinity, reduces porosity, improves thermal stability, and minimizes ion release. Despite the comprehensive analysis, this study has certain limitations. The investigation is limited to a specific range of Cr concentrations (0–5 wt.%) and a single calcination temperature (1000 °C). Advanced microstructural analysis techniques such as TEM or detailed surface chemistry studies are not included. Additionally, long-term stability and application-specific performance are not explored. The remainder of this paper is organized as follows: Section 2 describes the materials and experimental methods. Section 3 presents the results and discussion, including structural, thermal, and chemical analyses. Section 4 concludes the study by summarizing the key findings and potential applications of Cr-doped Al_2O_3 ceramic nanoparticles.

2. MATERIALS AND METHODS

2.1. Materials

Aluminum nitrate nonahydrate ($Al(NO_3)_3 \cdot 9H_2O$, MW = 375.13 g·mol^{-1}, purity ≥ 98%, Sigma-Aldrich) is used as the aluminum precursor. Chromium nitrate nonahydrate ($Cr(NO_3)_3 \cdot 9H_2O$, MW = 400.15 g·mol^{-1}, purity ≥ 98%, Sigma-Aldrich) served as the chromium dopant source. Citric acid ($C_6H_8O_7$, MW = 192.12 g·mol^{-1}, purity ≥ 99.5%, Sigma-Aldrich) is employed as a chelating and complexing agent in the sol–gel process. Deionized water is used as the solvent throughout the synthesis. Cr-doped Al_2O_3 samples with different chromium concentrations are prepared and labeled as AlCr0, AlCr1, AlCr3, and AlCr5, corresponding to 0, 1, 3, and 5 wt.% Cr, respectively.

2.2. Preparation of Cr-doped Al_2O_3 NPs

Cr-doped Al_2O_3 ceramic nanoparticles are synthesized using a citrate-based sol–gel method. Initially, an appropriate amount of aluminum nitrate corresponding to 0.1 mol of total metal ions is dissolved in approximately 100 mL of deionized water under continuous magnetic stirring to obtain a clear and homogeneous solution for the undoped sample (AlCr0). For the doped samples (AlCr1, AlCr3, and AlCr5), the total metal ion concentration is maintained at 0.1 mol, and suitable amounts of chromium nitrate are introduced to achieve the desired doping levels (1, 3, and 5 wt.% Cr). The required quantities of aluminum nitrate and chromium nitrate are dissolved together in deionized water under constant stirring to ensure uniform mixing of Al^{3+} and Cr^{3+} ions. Citric acid is then added gradually to each solution in a 1:1 molar ratio with the total metal ions (0.1 mol), acting as a chelating agent to form stable metal–citrate complexes and promote homogeneous distribution of the cations. The resulting mixture is heated at ~80 °C under continuous stirring until a transparent and stable sol is obtained. Further heating at the same temperature led to solvent evaporation and the transformation of the sol into a viscous gel. Upon continued heating, the gel underwent drying followed by spontaneous combustion, resulting in the formation of a porous precursor powder. This process involved the decomposition of nitrate–citrate complexes and the release of gaseous by-products such as H_2O, CO_2, and nitrogen oxides (NO_x). The obtained powder is allowed to cool to room temperature and then ground using an agate mortar and pestle to obtain a fine and homogeneous powder. The powder is further dried to eliminate residual moisture and reground to improve uniformity. Subsequently, the powders are compacted into pellets using a hydraulic press. The pellets are then sintered at 1000 °C in air, followed by natural cooling to room temperature. This high-temperature treatment facilitated phase formation, enhanced crystallinity, and improved densification of the Cr-doped Al_2O_3 ceramic nanoparticles. The final samples are labeled as AlCr0, AlCr1, AlCr3, and AlCr5, corresponding to 0, 1, 3, and 5 wt.% Cr, respectively, and are used for further characterization.

2.3. Characterization

The structural, physical, and thermal properties of the synthesized Al_2O_3:Cr ceramic nanoparticles (AlCr0–AlCr5) are systematically investigated using a range of analytical techniques. X-ray diffraction (XRD) analysis is performed to determine the crystal structure, phase composition, and crystallite size of the samples. The measurements are carried out using an X-ray diffractometer (PANalytical X'Pert PRO, Malvern Panalytical, Netherlands) with Cu Kα radiation (λ = 1.5406 Å), operating at 40 kV and 30 mA. The diffraction patterns are recorded over a 2θ range of 10°–90° with a step size of 0.02°. Fourier transform infrared (FTIR) spectroscopy is employed to identify functional groups and investigate chemical bonding within the samples. The spectra are recorded using a PerkinElmer Spectrum Two FTIR spectrometer (USA) in the wavenumber range of 400–4000 cm^{-1} with a resolution of 0.1 cm^{-1}. Raman spectroscopy is further utilized to examine vibrational modes and confirm the formation of the corundum structure. Raman measurements are conducted using a

Renishaw inVia Raman microscope (UK) with a laser excitation wavelength of 532 nm, and spectra are collected over the range of 100–1000 cm^{-1}. The physical properties, including bulk density and apparent porosity, are determined using the Archimedes method with distilled water as the immersion medium. The calculations are based on dry, soaked, and suspended weights of the samples. Thermal stability and decomposition behavior are analyzed using thermogravimetric analysis (TGA) and derivative thermogravimetry (DTG) with a TA Instruments Q500 thermal analyzer (USA). The measurements are conducted from room temperature up to 800 °C at a heating rate of 10 °C/min under a nitrogen atmosphere. Differential scanning calorimetry (DSC) is performed using a TA Instruments Q2000 system (USA) over a temperature range of 25–800 °C at a heating rate of 10 °C/min to investigate thermal transitions and crystallization behavior. Additionally, the release of Cr^{3+} ions from Al_2O_3:Cr ceramic nanoparticles is quantified using inductively coupled plasma optical emission spectroscopy (ICP-OES, PerkinElmer Optima 8000, USA) after one week of immersion. These characterization techniques collectively provided comprehensive insights into the structural, vibrational, physical, thermal, and chemical stability properties of the synthesized Cr-doped Al_2O_3 ceramic nanoparticles.

3. RESULTS AND DISCUSSION

3.1. Bulk density and apparent porosity

Figure 1 shows the variation of apparent porosity and bulk density of Al_2O_3 ceramic nanoparticles as a function of Cr nanoparticle (Cr NPs) addition (0–5 wt.%). A clear inverse relationship between porosity and density is observed across all samples. For the AlCr0 sample (Al_2O_3:Cr (0)), the material exhibits the highest apparent porosity (~28%) and the lowest bulk density (~3.20 g/cm^3). This indicates a relatively less compact microstructure with a higher volume of open pores, which is typical for pure alumina processed via sol–gel without sintering aids or dopants to enhance densification. With the introduction of 1 wt.% Cr (AlCr1, Al_2O_3:Cr (0.01)), there is a noticeable improvement in densification. The porosity decreases to ~26%, while the bulk density increases to ~3.24 g/cm^3. This suggests that a small amount of Cr acts as a sintering facilitator, promoting better particle packing and reducing pore volume. The Cr ions or nanoparticles likely enhance diffusion processes during high-temperature treatment (1000 °C). At 3 wt.% Cr (AlCr3, Al_2O_3:Cr (0.03)), the trend continues more significantly. The porosity drops further to ~24%, accompanied by an increase in density to ~3.30 g/cm^3. This composition appears to represent an optimal intermediate stage, where densification is substantially improved without introducing structural instability. The reduced pore fraction indicates improved grain bonding and more effective elimination of voids. For the 5 wt.% Cr sample (AlCr5, Al_2O_3:Cr (0.05)), the lowest apparent porosity (~22%) and highest bulk density (~3.35 g/cm^3) are achieved [43-45]. This confirms that increasing Cr content enhances densification and reduces pore connectivity. The higher density suggests a more compact and uniform microstructure, likely due to enhanced mass transport and grain rearrangement during sintering [46].

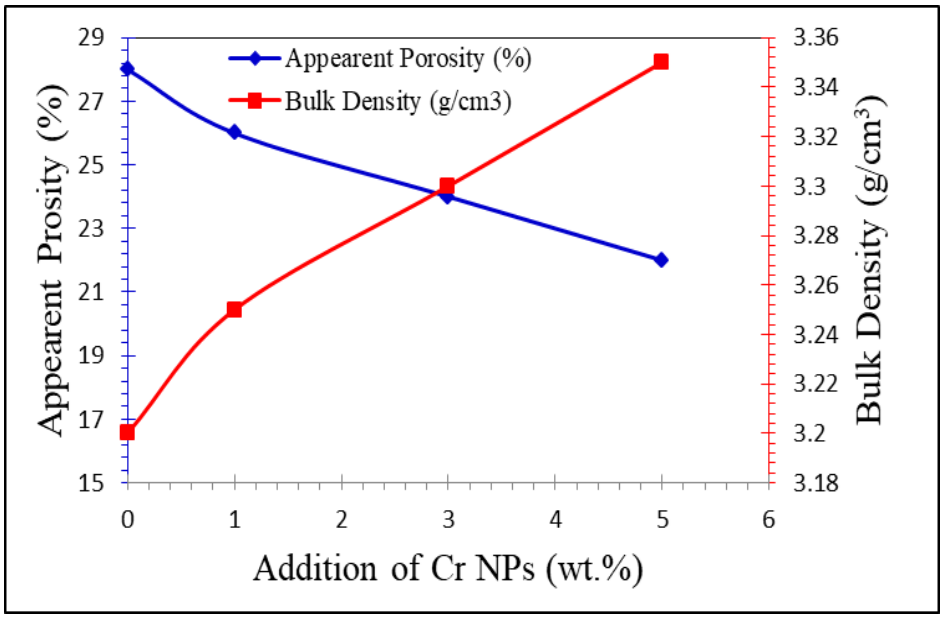

Figure 1 Variation of apparent porosity (%) and bulk density (g/cm³) of Al_2O_3:Cr ceramic nanoparticles (AlCr0, AlCr1, AlCr3, and AlCr5 corresponding to Cr contents of 0, 0.01, 0.03, and 0.05) as a function of Cr nanoparticle addition (0–5 wt.%), sintered at 1000 °C

3.2. XRD analysis

Based on Figure 2 and Table 1, the XRD patterns of all samples (AlCr0, AlCr1, AlCr3, and AlCr5) confirm that the synthesized powders are predominantly α-Al_2O_3 (alpha alumina). The diffraction peaks appearing at about 2θ = 25.6°, 35.1°, 37.8°, 43.4°, 52.6°, and 57.5° are indexed to the crystallographic planes (012), (104), (110), (113), (024), and (116), respectively. These reflections are characteristic of the corundum structure of α-Al_2O_3, indicating that the prepared ceramic nanoparticles have crystallized successfully after heat treatment. The absence of any extra diffraction peaks in the patterns suggests that no detectable secondary chromium oxide phase has formed, which implies that Cr is incorporated into the alumina lattice or remains highly dispersed below the XRD detection limit. The crystal structure identified from the diffraction pattern corresponds to α-Al_2O_3 with the corundum phase, generally matched with standard JCPDS/PDF card data for α-Al_2O_3. This phase belongs to the trigonal crystal system (often described in the hexagonal setting) with space group R-3c. The typical lattice parameters for α-Al_2O_3 are approximately a = b ≈ 4.76 Å and c ≈ 12.99 Å. In the commonly used hexagonal description, the cell angles are α = 90°, β = 90°, and γ = 120°. These values are consistent with the corundum structure and support the assignment of all major peaks to α-alumina. Since the peak positions in Figure 2 do not show any major shift with increasing Cr content, the basic crystal symmetry remains unchanged after doping, indicating that chromium addition does not alter the host phase structure significantly. A comparison between the samples shows that AlCr0 exhibits the same phase as the doped samples, but its peaks are relatively broader and less intense. This indicates a lower degree of crystallinity and a smaller crystallite size. Table 1 supports this observation, where the crystallite size values for AlCr0 range from about 20 to 30 nm, with an average around 25 nm. The broader full width at half maximum (FWHM) values in this sample suggest that the undoped alumina contains finer crystallites and probably more lattice imperfection or micro-strain compared with the Cr-doped compositions. For AlCr1, the diffraction peaks become sharper and slightly more intense than those of AlCr0, indicating improved crystallization after the addition of a small amount of chromium. The FWHM decreases, while the crystallite size increases to an average of about 29 nm. This result suggests that low-level Cr doping promotes crystal growth and improves structural

ordering. The retention of the same peak positions means that the host α-Al_2O_3 structure is preserved, while the improved peak quality reflects better atomic arrangement and enhanced grain development. The AlCr3 sample shows a further increase in peak sharpness and intensity. This confirms a continued improvement in crystallinity with increasing Cr concentration. According to Table 1, the crystallite size values increase further, and the average size is about 31–32 nm overall. The sample therefore appears to represent a more developed crystalline state than AlCr0 and AlCr1. The strengthening of the characteristic α-Al_2O_3 peaks without the appearance of impurity peaks indicates that this Cr content remains within the solubility or accommodation range of the alumina matrix under the present synthesis conditions. Among all samples, AlCr5 exhibits the sharpest and most intense diffraction peaks, indicating the highest crystallinity. Its FWHM values are the lowest, and the crystallite size reaches the largest values, ranging from about 30 to 43 nm, with an average of approximately 36 nm. This clearly shows that increasing Cr addition enhances crystal growth and reduces peak broadening. In other words, the structural ordering becomes progressively better from AlCr0 → AlCr1 → AlCr3 → AlCr5. The stronger and narrower peaks of AlCr5 suggest improved grain coalescence and reduced structural disorder after calcination at high temperature. The d-spacing values listed in Table 1 remain nearly constant for all samples, which is an important observation. It indicates that Cr incorporation does not cause a drastic distortion of the α-Al_2O_3 lattice. This is reasonable because chromium ions can substitute aluminum ions without strongly disrupting the host structure, especially at relatively low concentrations. Therefore, the main effect of Cr addition in these samples is not a phase transformation, but rather an enhancement in crystallinity and crystallite growth [47-50].

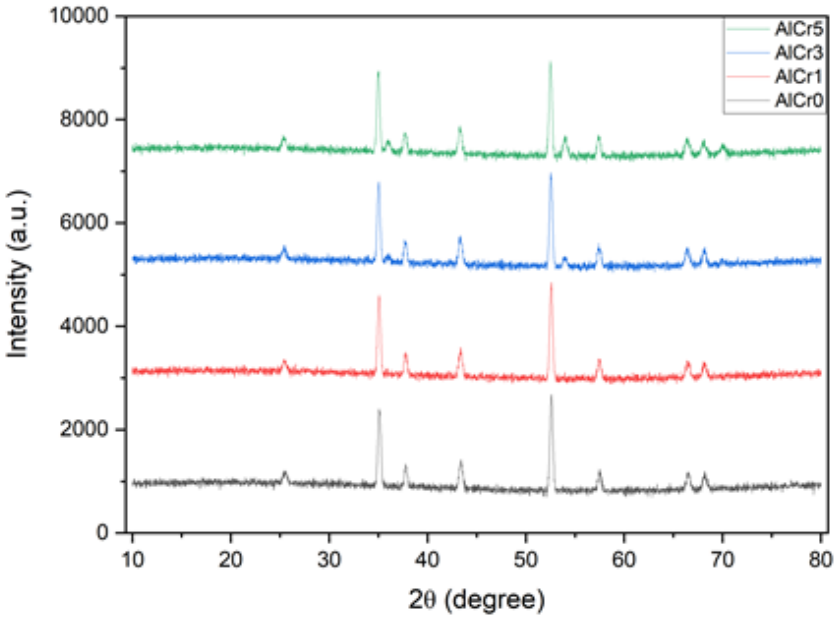

Figure 2 X-ray diffraction (XRD) patterns of Al_2O_3:Cr ceramic nanoparticles (AlCr0, AlCr1, AlCr3, and AlCr5) synthesized via sol–gel method and calcined at 1000 °C.

Table 1 Structural parameters of Al_2O_3:Cr ceramic nanoparticles (AlCr0–AlCr5).

Sample	2θ (°)	FWHM	(hkl)	d-spacing (Å)	Dcs (nm)	Dcs-avg (nm)
AlCr0	25.6	0.42	(012)	3.47	20	25
	35.1	0.38	(104)	2.55	23	
	37.8	0.36	(110)	2.38	25	
	43.4	0.34	(113)	2.08	27	
	52.6	0.32	(024)	1.74	29	
	57.5	0.31	(116)	1.60	30	
AlCr1	25.6	0.38	(012)	3.47	23	29
	35.1	0.34	(104)	2.55	27	
	37.8	0.32	(110)	2.38	29	
	43.4	0.30	(113)	2.08	31	
	52.6	0.29	(024)	1.74	33	
	57.5	0.28	(116)	1.60	34	
AlCr3	25.6	0.34	(012)	3.47	26	32
	35.1	0.30	(104)	2.55	30	
	37.8	0.28	(110)	2.38	33	
	43.4	0.27	(113)	2.08	35	
	52.6	0.26	(024)	1.74	36	
	57.5	0.25	(116)	1.60	28	
AlCr5	25.6	0.30	(012)	3.47	30	36
	35.1	0.27	(104)	2.55	34	
	37.8	0.25	(110)	2.38	37	
	43.4	0.24	(113)	2.08	39	
	52.6	0.23	(024)	1.74	41	
	57.5	0.22	(116)	1.60	43	

3.3. FTIR analysis

Figure 3 shows the FTIR spectra of Al_2O_3:Cr ceramic nanoparticles (AlCr0, AlCr1, AlCr3, and AlCr5) in the wavenumber range of 400–4000 cm^{-1}. The spectra of all samples exhibit similar characteristic absorption bands, confirming that the fundamental chemical structure of Al_2O_3 is preserved after Cr doping, with only slight variations in intensity and band position. For the AlCr0 sample, a broad absorption band observed around 3400 cm^{-1} is attributed to the stretching vibration of hydroxyl (–OH) groups, indicating the presence of adsorbed moisture on the surface of the nanoparticles. The band near 1600 cm^{-1} corresponds to the bending vibration of H–O–H, further confirming the presence of physically adsorbed water. In the lower wavenumber region, strong bands appearing around 500–800 cm^{-1} are assigned to Al–O stretching vibrations, which are characteristic of the Al_2O_3 lattice. These bands confirm the formation of alumina after calcination. With the addition of chromium in AlCr1, the FTIR spectrum retains all the characteristic bands of Al_2O_3, indicating that Cr incorporation does not introduce new functional groups. However, slight changes in band intensity and minor shifts can be observed, particularly in the Al–O vibration region (500–800 cm^{-1}). These variations suggest that Cr ions are interacting with the alumina lattice, possibly substituting Al^{3+} sites or occupying interstitial positions, leading to local structural distortions. For AlCr3, the spectral features become slightly more defined, especially in the metal–oxygen region. The Al–O bands appear sharper and more intense compared to AlCr0 and AlCr1, indicating improved structural ordering and crystallinity, which is consistent with the XRD results. The hydroxyl-related bands slightly decrease in intensity, suggesting reduced surface moisture due to better densification and grain growth at higher Cr content. In the case of AlCr5, the FTIR spectrum shows the most pronounced and well-defined Al–O absorption bands,

confirming enhanced crystallinity and stronger metal–oxygen bonding. The broad –OH band around 3400 cm^{-1} is further reduced in intensity, indicating a decrease in adsorbed water content. This behavior suggests that higher Cr doping leads to a more compact and less porous structure, consistent with the density and porosity results discussed earlier. No additional peaks corresponding to chromium oxide phases are observed, supporting the conclusion that Cr is well incorporated into the Al_2O_3 matrix without forming separate phases. Table 2 presents the FTIR band positions and their corresponding vibrational assignments of Al_2O_3:Cr ceramic nanoparticles (AlCr0–AlCr5), highlighting the presence of hydroxyl groups and characteristic Al–O bonding [51, 52].

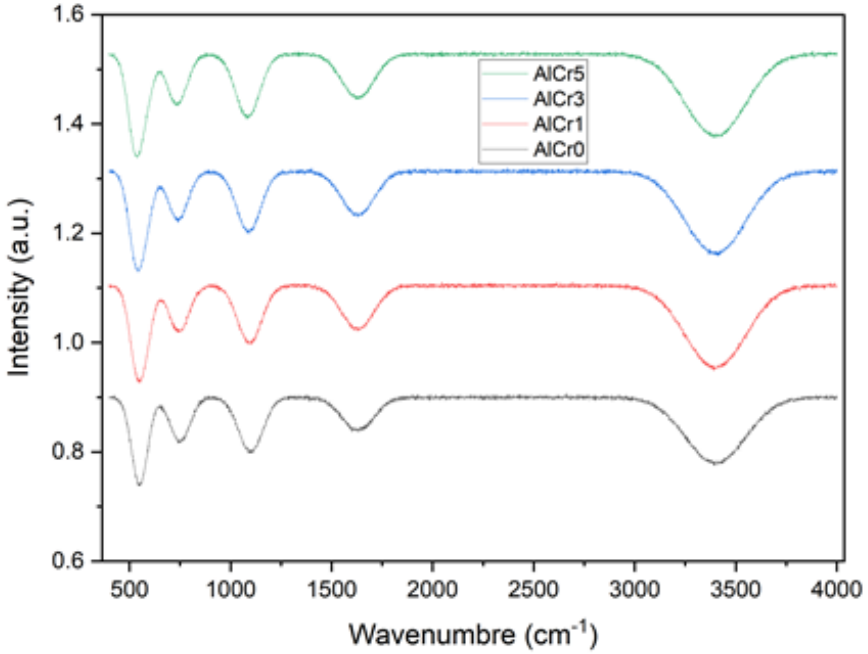

Figure 3 FTIR spectra of Al_2O_3:Cr ceramic nanoparticles (AlCr0, AlCr1, AlCr3, and AlCr5).

Table 2 FTIR band assignments of Al_2O_3:Cr ceramic nanoparticles (AlCr0–AlCr5).

Sample	Wavenumber (cm^{-1})	Assignment	Description
AlCr0	~3400	O–H stretching	Adsorbed / hydroxyl groups
	~1600	H–O–H bending	Molecular water
	1000–1100	Al–O / Al–O–H	Residual precursor or lattice vibration
	500–800	Al–O stretching	Characteristic alumina vibration
AlCr1	~3400	O–H stretching	Reduced intensity (less moisture)
	~1600	H–O–H bending	Weak water band
	1000–1100	Al–O vibration	Slight shift due to Cr doping
	500–800	Al–O stretching	Enhanced intensity
AlCr3	~3400	O–H stretching	Further reduced
	~1600	H–O–H bending	Weak
	1000–1100	Al–O vibration	Improved structural order
	500–800	Al–O stretching	Sharper peaks
AlCr5	~3400	O–H stretching	Minimum intensity
	~1600	H–O–H bending	Very weak
	1000–1100	Al–O vibration	Stable
	500–800	Al–O stretching	Strong and well-defined

3.4. Raman analysis

Figure 4 presents the Raman spectra of Al_2O_3:Cr ceramic nanoparticles (AlCr0, AlCr1, AlCr3, and AlCr5) in the range of 100–1200 cm^{-1}. All samples exhibit well-defined Raman active modes characteristic of the α-Al_2O_3 (corundum) structure, confirming the results obtained from XRD analysis. The observed peaks around ~380–420 cm^{-1}, ~450 cm^{-1}, ~580 cm^{-1}, and ~630–650 cm^{-1} correspond to the typical vibrational modes of α-alumina, including Eg and A1g symmetry modes. For the AlCr0 sample, the Raman peaks are present but relatively broader and of lower intensity, indicating a lower degree of crystallinity and smaller crystallite size. The bands around ~418 cm^{-1} and ~645 cm^{-1} are associated with bending and stretching vibrations of the Al–O bonds in the corundum lattice. The relatively broad nature of these peaks suggests structural disorder and possible lattice strain in the undoped sample. With the addition of chromium in AlCr1, the Raman peaks become sharper and more intense compared to AlCr0. This indicates an improvement in crystallinity and structural ordering. The positions of the peaks remain nearly unchanged, confirming that the incorporation of Cr does not alter the fundamental crystal structure of α-Al_2O_3. However, slight changes in peak intensity suggest that Cr ions influence the local bonding environment within the lattice. For AlCr3, the Raman spectra show further enhancement in peak sharpness and intensity. The vibrational modes become more well-defined, indicating improved long-range order and reduced lattice defects. This behavior is consistent with the XRD and FTIR results, which showed increased crystallite size and better structural organization at this doping level. The absence of additional peaks indicates that no secondary chromium oxide phases are formed. The AlCr5 sample exhibits the highest Raman intensity and the sharpest peaks among all samples, indicating the highest degree of crystallinity. The strong and well-resolved Raman modes confirm enhanced lattice ordering and reduced structural defects. The increased intensity can also be attributed to improved grain growth and reduced phonon scattering due to fewer defects. No new Raman bands related to chromium oxide phases are observed, confirming that Cr is successfully incorporated into the alumina lattice without forming separate phases. A comparison among all samples clearly shows that the Raman peak intensity increases and peak width decreases in the order: AlCr0 < AlCr1 < AlCr3 < AlCr5, which indicates progressive improvement in crystallinity and structural quality with increasing Cr content [53-55]. Table 3 presents the Raman active modes of Al_2O_3:Cr samples, including the observed Raman shift positions and their assignments to Eg and A1g vibrational modes associated with the corundum structure.

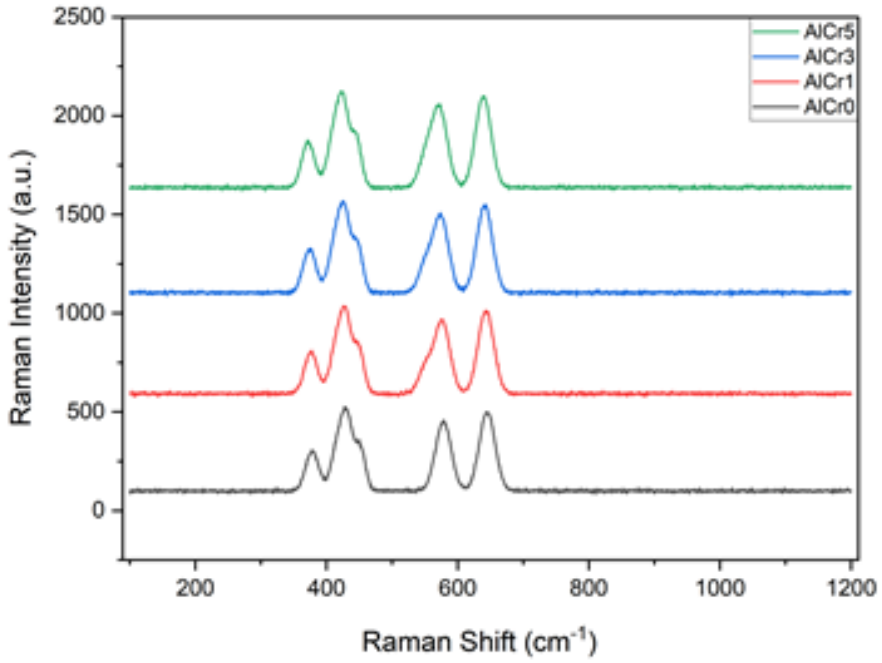

Figure 4 Raman spectra of Al_2O_3:Cr ceramic nanoparticles (AlCr0, AlCr1, AlCr3, and AlCr5).

Table 3 Raman band positions and assignments of Al_2O_3:Cr ceramic nanoparticles (AlCr0–AlCr5).

Sample	Raman Shift (cm^{-1})	Mode	Assignment
AlCr0	~380	Eg	Lattice vibration (Al–O)
	~418	Eg	Bending mode of Al–O
	~450	A1g	Symmetric vibration
	~580	Eg	Al–O stretching
	~645	A1g	Strong Al–O stretching
AlCr1	~380	Eg	Lattice vibration
	~420	Eg	Al–O bending
	~450	A1g	Symmetric mode
	~580	Eg	Stretching vibration
	~645	A1g	Strong Al–O mode
AlCr3	~380	Eg	Lattice vibration
	~420	Eg	Bending vibration
	~450	A1g	Symmetric mode
	~580	Eg	Al–O stretching
	~645	A1g	Strong mode
AlCr5	~380	Eg	Lattice vibration
	~420	Eg	Bending mode
	~450	A1g	Symmetric vibration
	~580	Eg	Stretching
	~645	A1g	Strong Al–O vibration

3.5. TGA analysis

Figure 5 shows the thermogravimetric analysis (TGA) curves of Al_2O_3:Cr ceramic nanoparticles (AlCr0, AlCr1, AlCr3, and AlCr5) in the temperature range from room temperature to 1000 °C. All samples exhibit a similar weight loss trend with increasing temperature, indicating comparable thermal decomposition behavior, although slight differences are observed depending on Cr content. For the AlCr0 sample, an initial weight loss occurs below ~150 °C, which is attributed to the removal of physically adsorbed water and surface hydroxyl groups. A second, more gradual weight loss is observed between ~200–400 °C, corresponding to the decomposition of residual organic species or precursor remnants from the sol–gel process. Beyond 400 °C, the weight becomes relatively stable, indicating the formation of thermally stable Al_2O_3. The total weight loss for AlCr0 is the highest among all samples, suggesting a higher amount of residual moisture and organic content. With the introduction of chromium in AlCr1, a similar two-step weight loss behavior is observed; however, the total weight loss is slightly reduced compared to AlCr0. This indicates that Cr incorporation improves the thermal stability of the material and promotes more complete decomposition of volatile species during synthesis. The stabilization region above 400 °C is reached more rapidly, reflecting improved structural consolidation. For the AlCr3 sample, the weight loss further decreases, and the curve becomes flatter at high temperatures. This suggests enhanced thermal stability and reduced presence of volatile components. The improved behavior can be attributed to stronger bonding within the Al_2O_3 lattice due to Cr incorporation, which reduces the number of surface hydroxyl groups and residual impurities. The AlCr5 sample exhibits the lowest overall weight loss and the most stable behavior across the entire temperature range. The initial moisture loss is minimal, and the decomposition of residual species is significantly reduced. The curve becomes nearly constant beyond ~400 °C, indicating excellent thermal stability. This behavior confirms that higher Cr content leads to a more compact and stable ceramic structure with fewer volatile components. A comparison among all samples reveals that the total weight loss decreases in the order: AlCr0 > AlCr1 > AlCr3 > AlCr5, indicating that Cr doping enhances thermal stability. The reduced weight loss at higher doping levels is consistent with the FTIR results (lower hydroxyl content) and XRD results (improved crystallinity). Thus, Cr incorporation strengthens the alumina network, reduces defects, and improves resistance to thermal decomposition [56, 57]. Table 4 presents the thermal parameters of Al_2O_3:Cr ceramic nanoparticles, including weight loss percentages in different temperature regions and the residual mass at high temperature, indicating the effect of Cr doping on thermal stability.

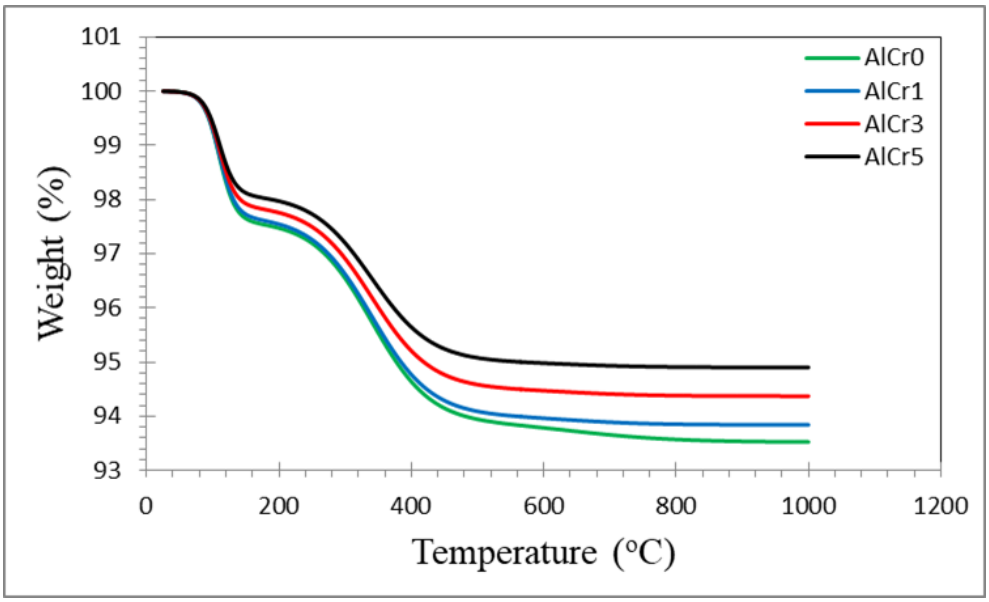

Figure 5 Thermogravimetric analysis (TGA) curves of Al_2O_3:Cr ceramic nanoparticles (AlCr0, AlCr1, AlCr3, and AlCr5).

Table 4 Thermal parameters of Al_2O_3:Cr ceramic nanoparticles (AlCr0–AlCr5).

Sample	Initial weight loss (%) (RT–150 °C)	Weight loss (%) (150–400 °C)	Total weight loss (%)	Residual weight at 1000 °C (%)
AlCr0	~2.2	~3.8	~6.0	~94.0
AlCr1	~2.0	~3.5	~5.5	~94.5
AlCr3	~1.8	~3.2	~5.0	~95.0
AlCr5	~1.5	~2.8	~4.3	~95.7

3.6. DSC analysis

Figure 6 shows the differential scanning calorimetry (DSC) curves of Al_2O_3:Cr ceramic nanoparticles (AlCr0, AlCr1, AlCr3, and AlCr5) over a wide temperature range. All samples exhibit two main thermal events: an endothermic peak at low temperature (~100–200 °C) and a prominent exothermic peak at higher temperature (~750–900 °C). These thermal features provide insight into the phase evolution and thermal behavior of the materials. For the AlCr0 sample, the endothermic peak observed around ~120–150 °C is attributed to the removal of physically adsorbed water and dehydration of surface hydroxyl groups. This is consistent with the TGA and FTIR results, which confirmed the presence of moisture in the undoped sample. The broad exothermic peak centered around ~800 °C corresponds to the phase transformation and crystallization of amorphous alumina into the stable α-Al_2O_3 phase. The relatively lower intensity and broader nature of this peak indicate slower crystallization kinetics and lower structural ordering. With the addition of chromium in AlCr1, the endothermic peak slightly decreases in intensity, suggesting reduced moisture content due to improved particle packing and reduced porosity. The exothermic peak shifts slightly toward a higher temperature and becomes sharper, indicating enhanced crystallization behavior. This suggests that Cr acts as a facilitator for structural rearrangement, improving the transformation process. For the AlCr3 sample, the endothermic peak becomes less pronounced, confirming further reduction in hydroxyl content and improved thermal stability. The exothermic peak becomes sharper and more intense, indicating more efficient and well-defined crystallization. The shift in peak position suggests that the presence of Cr

modifies the energy required for phase transformation, likely due to lattice interactions and improved diffusion during heating. The AlCr5 sample exhibits the most distinct thermal behavior among all samples. The endothermic peak is minimal, indicating very low moisture and residual content. The exothermic peak is the sharpest and most intense, and it is slightly shifted compared to the undoped sample. This reflects enhanced crystallization kinetics and improved structural ordering, consistent with XRD and Raman results showing higher crystallinity for this sample. The sharper peak also indicates a more uniform phase transformation. A comparison between all samples shows that the endothermic peak intensity decreases and the exothermic peak becomes sharper and more defined with increasing Cr content. This indicates that Cr doping reduces residual volatile species and enhances the crystallization process. The shift and sharpening of the exothermic peak confirm that chromium improves the thermal behavior and promotes the formation of a well-ordered α-Al_2O_3 phase [58, 59]. Table 5 presents the DSC-derived thermal parameters of Al_2O_3:Cr ceramic nanoparticles, including the temperatures of endothermic and exothermic peaks and their corresponding thermal behavior, illustrating the effect of Cr doping on crystallization and thermal stability.

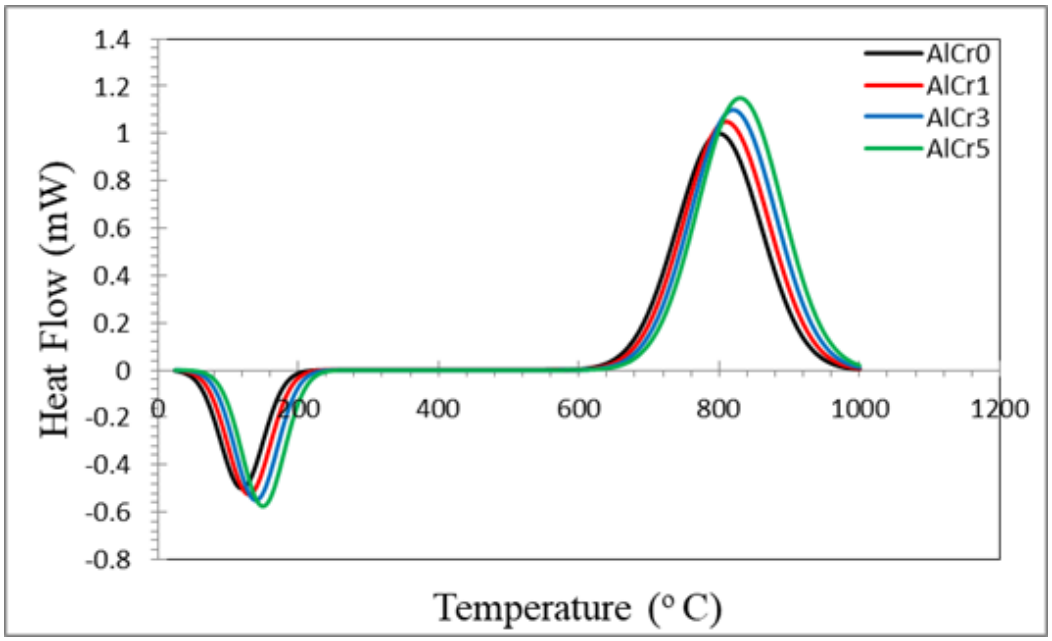

Figure 6 Differential scanning calorimetry (DSC) curves of Al_2O_3:Cr ceramic nanoparticles (AlCr0, AlCr1, AlCr3, and AlCr5).

Table 5 DSC thermal parameters of Al_2O_3:Cr ceramic nanoparticles (AlCr0–AlCr5).

Sample	Endothermic peak (°C)	Exothermic peak (°C)	Peak intensity (mW)	Thermal behavior
AlCr0	~130	~800	Moderate	Slower crystallization
AlCr1	~140	~810	Moderate–high	Improved transformation
AlCr3	~145	~820	High	Enhanced crystallization
AlCr5	~150	~830	Highest	Best thermal stability and ordering

3.7. DTG analysis

Figure 7 shows the derivative thermogravimetric (DTG) curves of Al_2O_3:Cr ceramic nanoparticles (AlCr0, AlCr1, AlCr3, and AlCr5) as a function of temperature. The DTG curves provide a more

precise identification of the temperatures at which maximum weight loss occurs, highlighting the decomposition stages observed in TGA. For the AlCr0 sample, two distinct negative peaks are observed. The first sharp peak centered around ~100–150 °C corresponds to the maximum rate of weight loss due to the removal of physically adsorbed water and surface hydroxyl groups. The second broader peak around ~250–400 °C is attributed to the decomposition of residual organic compounds and precursor remnants from the sol–gel process. The relatively higher (intensity) of these peaks indicates that AlCr0 contains a larger amount of volatile species and exhibits lower thermal stability. With the addition of chromium in AlCr1, both DTG peaks decrease slightly in intensity, indicating a reduction in the rate of weight loss. This suggests that Cr incorporation reduces the amount of adsorbed moisture and organic residues. The peak positions remain nearly unchanged, confirming that the decomposition mechanism is similar, but the extent of decomposition is reduced compared to the undoped sample. For the AlCr3 sample, the DTG peaks become further reduced and slightly broadened, indicating a more gradual and controlled decomposition process. The lower peak intensity reflects improved thermal stability and reduced volatile content. This behavior suggests that Cr doping enhances the structural integrity of the material and limits rapid mass loss during heating. The AlCr5 sample exhibits the lowest DTG peak intensities among all samples. The first peak associated with moisture removal is significantly reduced, indicating minimal adsorbed water. The second peak corresponding to organic decomposition is also less pronounced, confirming that the sample contains fewer residual impurities. The smoother DTG curve indicates a more stable and gradual thermal decomposition process. A comparison among all samples shows that the maximum rate of weight loss decreases in the order: AlCr0 > AlCr1 > AlCr3 > AlCr5. This clearly demonstrates that increasing Cr content enhances thermal stability and reduces the presence of volatile components. Additionally, the slight broadening and reduction in peak indicate a more controlled decomposition process at higher doping levels [60, 61]. Table 6 presents the DTG-derived thermal parameters of Al_2O_3:Cr ceramic nanoparticles, including the temperatures of maximum weight loss and corresponding peak intensities, highlighting the effect of Cr doping on decomposition behavior and thermal stability.

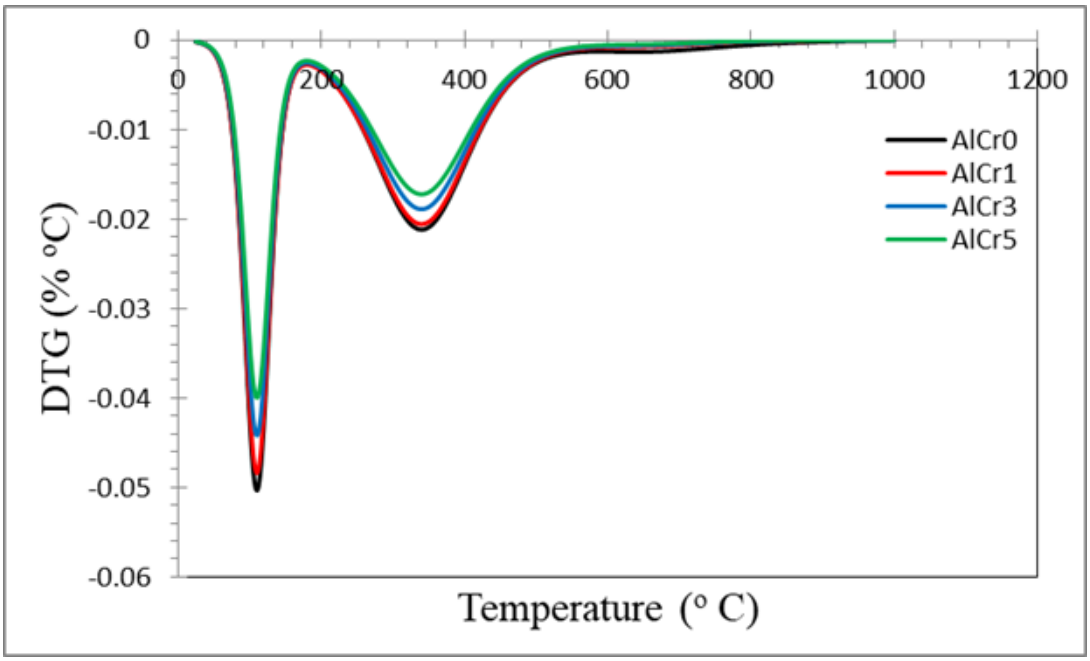

Figure 7 Derivative thermogravimetric (DTG) curves of Al_2O_3:Cr ceramic nanoparticles (AlCr0, AlCr1, AlCr3, and AlCr5).

Table 6 DTG thermal parameters of Al_2O_3:Cr ceramic nanoparticles (AlCr0–AlCr5).

Sample	Peak 1 temperature (°C)	Peak 2 temperature (°C)	DTG peak intensity (%/°C)	Interpretation
AlCr0	~120	~320	Highest	Rapid decomposition, low stability
AlCr1	~125	~330	High	Improved stability
AlCr3	~130	~340	Moderate	Controlled decomposition
AlCr5	~135	~350	Lowest	Highest thermal stability

3.8. ICP-OES analysis of Cu^{3+} ion release from Al_2O_3:Cr ceramic NPs

Figure 8 illustrates the ion concentration released (ppm) from Al_2O_3:Cr ceramic nanoparticles (AlCr0, AlCr1, AlCr3, and AlCr5). A clear decreasing trend in ion release is observed with increasing Cr content, indicating improved chemical stability of the material upon doping. For the AlCr0 sample, the highest ion release value (~0.007 ppm) is recorded. This suggests that the undoped Al_2O_3 exhibits relatively lower chemical stability and a higher tendency for surface ion leaching. The higher ion release can be attributed to its higher porosity and lower density, as previously observed, which facilitate interaction with the surrounding medium and promote ion diffusion. With the introduction of chromium in AlCr1, the ion release decreases to approximately ~0.0055 ppm. This reduction indicates that Cr doping enhances the structural integrity of the material, reducing its susceptibility to ion leaching. The improved densification and reduced pore volume limit the pathways available for ion diffusion. For the AlCr3 sample, the ion concentration further decreases to around ~0.003 ppm. This significant reduction reflects enhanced chemical stability and stronger bonding within the alumina matrix. The improved crystallinity and reduced defect concentration, as confirmed by XRD and Raman analyses, contribute to minimizing ion release. The AlCr5 sample exhibits the lowest ion release (~0.002 ppm), indicating the highest chemical stability among all samples. The dense microstructure, reduced porosity, and improved grain bonding effectively suppress ion diffusion and leaching. This behavior confirms that higher Cr content leads to a more stable and durable ceramic structure. A comparison among all samples reveals that ion release decreases in the order: AlCr0 > AlCr1 > AlCr3 > AlCr5, demonstrating that Cr incorporation significantly enhances the chemical resistance of Al_2O_3 ceramic nanoparticles. The reduction in ion release correlates well with the improvements in density, crystallinity, and thermal stability observed in previous analyses [62].

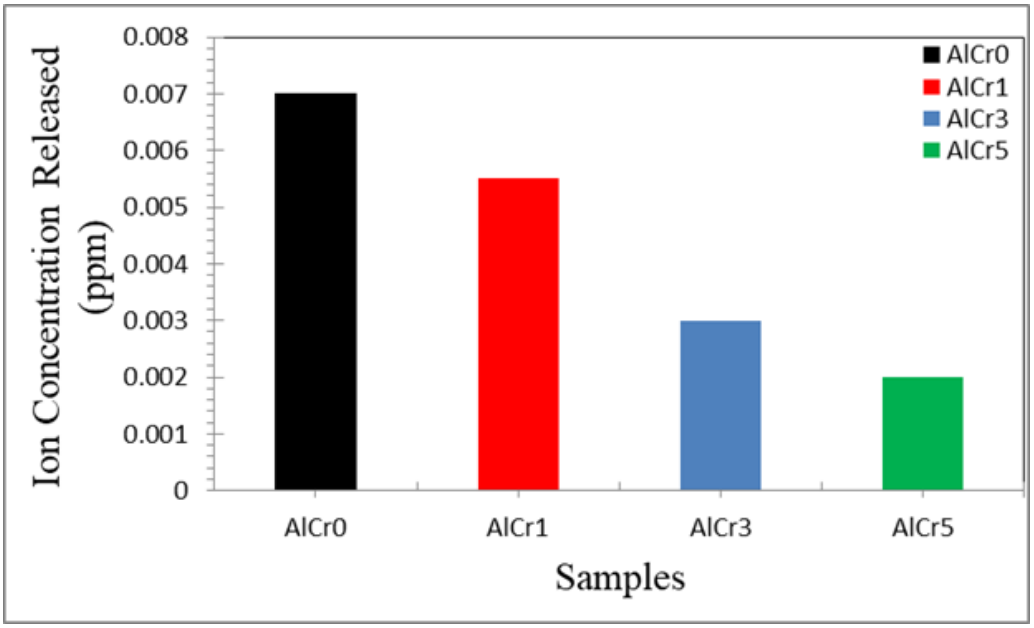

Figure 8 Ion concentration released (ppm) from Al_2O_3:Cr ceramic nanoparticles (AlCr0, AlCr1, AlCr3, and AlCr5)

4. CONCLUSIONS

In this study, Cr-doped Al_2O_3 (Al_2O_3:Cr) ceramic nanoparticles (AlCr0–AlCr5) were successfully synthesized via the sol–gel method and calcined at 1000 °C. XRD analysis confirmed the formation of a single-phase α- Al_2O_3 (corundum structure) for all samples, with no detectable secondary phases, indicating effective incorporation of Cr into the alumina lattice. A progressive decrease in FWHM and increase in crystallite size from ~25 nm to ~36 nm was observed with increasing Cr content, demonstrating enhanced crystallinity and grain growth. FTIR and Raman analyses further supported the formation of Al–O bonding and the preservation of the corundum structure, while revealing improved structural ordering with Cr addition. The reduction in hydroxyl-related bands and sharper Raman peaks confirmed decreased surface defects and enhanced lattice stability. Thermal analyses (TGA, DSC, and DTG) showed that all samples exhibit good thermal stability above 400 °C, with Cr doping significantly reducing weight loss and enhancing crystallization behavior. The AlCr5 sample displayed the highest thermal stability and most efficient phase transformation. Density and porosity measurements revealed that increasing Cr content improves densification, as evidenced by higher bulk density and reduced apparent porosity. Furthermore, ICP-OES results demonstrated a composition-dependent decrease in Cr^{3+} ion release, indicating enhanced chemical stability with higher Cr concentrations. Cr doping effectively improves the structural, thermal, and chemical properties of Al_2O_3 ceramic nanoparticles without altering the fundamental crystal structure. Among all samples, AlCr5 exhibited the best overall performance, making it a promising candidate for advanced ceramic applications requiring high stability and durability.

References

[1] M. M. Najim, B. A. Yousif, The Iraqi Geological Journal 11 (2021) 2 https://doi.org/10.46717/igj.54.1a.3ms-2021-01-24
[2] M. M. Najim, B. A. Yousif, The Iraqi Geological Journal 13 (2020) 49 https://doi.org/10.46717/igj.53.2f.4ms-2020-12-27
[3] Mojahid Mohammed Najim and Lubna Jaleil Ibraheim, AIP Conference Proceedings 1 (2020) 99 https://doi.org/10.1063/5.0000327
[4] H. M. Abdullah, M. M. Najim, B. A. Yousif, Experimental and Theoretical NANOTECHNOLOGY 9 (2025) 67 https://doi.org/10.56053/9.s.67
[5] H. M. Abdullah, M. M. Najim, B. A. Yousif, Experimental and Theoretical NANOTECHNOLOGY 9 (2025) 39 https://doi.org/10.56053/9.s.39
[6] Ban A.Yousif, Al-œNahrain journal of science 25 (2022) 49 https://doi.org/10.22401/anjs.25.4.08
[7] Al-Hussein, Elham Talib Abd, Yousif, Ban A. AIP Conference Proceedings 2213 (2020) 020199 https://doi.org/10.1063/5.0000328
[8] Khalef Wafaa K. et al., International Journal of Nanoelectronics and Materials, 11 (2018) 23 https://doi.org/2-s2.0-85069679313
[9] I. Alshalal, H. M. I. Al-Zuhairi, A. A. Abtan, M. Rasheed, M. K. Asmail. J. Mech. Behav. Mater. 32 (2023) 1 https://doi.org/10.1515/jmbm-2022-0280
[10] M. Sellam, M. Rasheed, S. Azizi, T. Saidani. Ceram. Int. 50 (2024) 20917 https://doi.org/10.1016/j.ceramint.2024.03.094
[11] O. Alabdali, S. Shihab, M. Rasheed, T. Rashid. 3rd inter. Scient. conf. alkafeel univ. (ISCKU 2021) 39 (2022) 77 https://doi.org/10.1063/5.0066860
[12] M. Rasheed, O. Alabdali, S. Shihab, A. Rashid, T. Rashid, J. Phys.: Conf. Ser. 1999 (2021) 012078 https://doi.org/10.1088/1742-6596/1999/1/012078
[13] N. Assoudi et al. *Opt. Quant. Electron.* 54 (2022) 9 https://doi.org/10.1007/s11082-022-03927-x
[14] R. Jalal, S. Shihab, M.A. Alhadi, M. Rasheed, J. Phys.: Conf. Ser. 1660 (2020) 012090 https://doi.org/10.1088/1742-6596/1660/1/012090
[15] S. Shihab, M. Rasheed, O. Alabdali, A.A. Abdulrahman, J. Phys.: Conf. Ser. 1879 (2021) 022120. https://doi.org/10.1088/1742-6596/1879/2/022120
[16] A. Keziz, M. Heraiz, M. RASHEED, A. Oueslati. Mater Chem. Phys. 325 (2024) 129757 https://doi.org/10.1016/j.matchemphys.2024.129757
[17] D. Kherifi, A. Keziz, M. Rasheed, A. Oueslati. Ceram. Int. 50 (2024) 30175 https://doi.org/10.1016/j.ceramint.2024.05.317
[18] A. Jaber, M. Ismael, T. Rashid, M. A. Sarhan, M. Rasheed, I. M. Sala. Eureka: Phys. Eng. 4 (2023) 29 https://doi.org/10.21303/2461-4262.2023.002770
[19] T. Rashid, M. M. Mokji, M. Rasheed. J. Optics 66 (2024) 99 https://doi.org/10.1007/s12596-024-02080-w
[20] H. K. Aity, E. Dhahri, M. Rasheed. Ceram. Int. 50 (2024) 54666 https://doi.org/10.1016/j.ceramint.2024.10.324
[21] M. Rasheed, S. Shihab, O. Alabdali, A. Rashid, T. Rashid, J. Phys.: Conf. Ser. 1999 (2021) 012077 https://doi.org/10.1088/1742-6596/1999/1/012077
[22] M. Rasheed, M. Nuhad Al-Darraji, S. Shihab, A. Rashid, T. Rashid. J. Phys.: Conf. Ser. 1963 (2021) 012058 https://doi.org/10.1088/1742-6596/1963/1/012058
[23] A. Keziz, M. Heraiz, F. Sahnoune, M. Rasheed, Ceram. Int. 49 (2023) 32989 https://doi.org/10.1016/j.ceramint.2023.07.275
[24] E. Kadri, K. Dhahri, R. Barillé, M. Rasheed. Phase Transi. 94 (2021) 65 https://doi.org/10.1080/01411594.2020.1832224

[25] D. Bouras, M. Rasheed, Opt. Quantum Electron. 54 (2022) 12 https://doi.org/10.1007/s11082-022-04161-1
[26] A. Zubaidi, L.M. Asaad, I. Alshalal, M. Rasheed, J. Mech. Behav. Mater. 32 (2023) 1 https://doi.org/10.1515/jmbm-2022-0302
[27] M. Rasheed et al., J. Phys.: Conf. Ser. 1999 (2021) 012080 https://doi.org/10.1088/1742-6596/1999/1/012080
[28] M. Rasheed, M.N. Al-Darraji, S. Shihab, A. Rashid, T. Rashid, J. Phys.: Conf. Ser. 1963 (2021) 012059 https://doi.org/10.1088/1742-6596/1963/1/012059
[29] M. Enneffatia, M. Rasheed, B. Louati, K. Guidara, S. Shihab, R. Barillé, J. Phys.: Conf. Ser. 1795 (2021) 012050 https://doi.org/10.1088/1742-6596/1795/1/012050
[30] M. Rasheed, O.Y. Mohammed, S. Shihab, A. Al-Adili, J. Phys.: Conf. Ser. 1795 (2021) 012043 https://doi.org/10.1088/1742-6596/1795/1/012043
[31] A.H. Ali, A.S. Jaber, M.T. Yaseen, M. Rasheed, O. Bazighifan, T.A. Nofal, Complexity 2022 (2022) 1 https://doi.org/10.1155/2022/9367638
[32] M. Rasheed, et al., J. Adv. Biotechnol. Exp. Ther. 6 (2023) 495 https://doi.org/10.5455/jabet.2023.d144
[33] M. Rasheed, I. Alshalal, A.A. Ashed, M.A. Sarhan, A.S. Jaber, Indones. J. Electr. Eng. Comput. Sci. 33 (2024) 653 https://doi.org/10.11591/ijeecs.v33.i1.pp653-660
[34] I.M. Mohammed, M. Rasheed, AIP Conf. Proc. 3321 (2025) 020026 https://doi.org/10.1063/5.0289719
[35] F. Boudou, A. Belakredar, A. Berkane, M. Rasheed. Not. Sci. Biol. 17 (2025) 12183 https://doi.org/10.55779/nsb17212183
[36] F. Boudou, et al., Not. Sci. Biol. 17 (2025) 12593 https://doi.org/10.55779/nsb17312593
[37] F. Boudou, A. Guendouzi, A. Belkredar. M. Rasheed, Not. Sci. Biol. 16 (2024) 13837 https://doi.org/10.55779/nsb16211837
[38] R.S. Mahmood et al. J. Mech. Behav. Mater. 34 (2025) 1 https://doi.org/10.1515/jmbm-2025-0040
[39] T. Rashid, M.M. Mokji, M. Rasheed, J. Mech. Behav. Mater. 34 (2025) 77 https://doi.org/10.1515/jmbm-2025-0074
[40] M. Rasheed, M. N. Mohammedali, F. A. Sadiq, M. A. Sarhan, T. Saidani. J. Optics (New Delhi. Print) (2024) https://doi.org/10.1007/s12596-024-01928-5
[41] A.J. Hussein, M.N. Al-Darraji, M. Rasheed, M.A. Sarhan, IOP Conf. Ser.: Earth Environ. Sci. 1262 (2023) 022007 https://doi.org/ 10.1088/1755-1315/1262/2/022007
[42] A.J. Hussein, M.N. Al-Darraji, M. Rasheed, M.A. Sarhan, IOP Conf. Ser.: Earth Environ. Sci. 1262 (2023) 022005. https://doi.org/10.1088/1755-1315/1262/2/022005
[43] T. Saidani, M. Rasheed, I. Alshalal, A.A. Rashed, M.A. Sarhan, R. Barillé, Res. Eng. Struct. Mater. 10 (2024) 743 http://dx.doi.org/10.17515/resm2023.21ma0922rs
[44] M. A. Sarhan, S. Shihab, B. E. Kashem, M. Rasheed, J. Phy.: Conf. Ser., 1879 (2021) 022122 https://doi.org/10.1088/1742-6596/1879/2/022122
[45] M. Rasheed, O. Alabdali, S. Shihab, J. Phy.: Conf. Ser. 1879 (2021) 032120 https://doi.org/10.1088/1742-6596/1879/3/032120
[46] M. Rasheed, R. Barillé, J. Non-Cryst. Solids., 476 (2017) 1 https://doi.org/10.1016/j.jnoncrysol.2017.04.027
[47] M. Rasheed, R. Barillé, Opt. Quantum Electron. 49 (2017) 61 https://doi.org/10.1007/s11082-017-1030-7
[48] F. Dkhilalli, S. M. Borchani, M. Rasheed, R. Barille, K. Guidara, M. Megdiche, J. Mater. Sci. Mater. Electron, 29 (2018) 6297 https://doi.org/10.1007/s10854-018-8609-z
[49] A. Boumezoued, K. Guergouri, Régis Barillé, Rechem Djamil, Mourad Zaabat, M. Rasheed, J. Alloys Compd. 791 (2019) 550 https://doi.org/10.1016/j.jallcom.2019.03.251
[50] N. Ben Azaza et al., Opt. Mater., 96 (2019) 109328 https://doi.org/10.1016/j.optmat.2019.109328

[51] Areej Adnan Hateef, Essebti Dhahri, M. Rasheed, Habiba Kadhim, Z. Abbas, N. Hassan, Study of the influence concentration difference of copper in properties of cerium nanopowder, Physics and Chemistry of Solid State 25 (2024) 801 https://doi.org/10.15330/pcss.25.4.801-810
[52] M. Rasheed, SuhaShihab, O. Alabdali, H. H. Hassan, J. Phys. Conf. Ser., 1879 (2021) 032113 https://doi.org/10.1088/1742-6596/1879/3/032113
[53] H. K. Aity, M. Rasheed, E. Dhahri, A. A. Hateef, T. Saidani, Chromium-doped magnesium oxide nanoparticles: dielectric insights and antibacterial potentials, Journal of Materials Science, 61 (2026) 6226 https://doi.org/10.1007/s10853-026-12241-w
[54] T. Saidani, S. Mokhtari, M. Rasheed, H. Lahmar, M. Trari, Annealing temperature dependent properties ZnO–TiO_2 bilayer thin films: characteristics and photocatalytic activity, Journal of the Indian Chemical Society 103 (2026) 102499 https://doi.org/10.1016/j.jics.2026.102499
[55] M. RASHEED, A. Khaleefah, Materials Chemistry and Physics, 353 (2026) 132112 https://doi.org/10.1016/j.matchemphys.2026.132112
[56] S. S. Batros, M. Rasheed, H. K. Aity, A. A. Hatef, T. Saidani, Materials Chemistry and Physics, 355 (2026) 132243 https://doi.org/10.1016/j.matchemphys.2026.132243
[57] A. Raghdi, M. Heraiz, M. Rasheed, A. Keziz, Investigation of halloysite thermal decomposition through differential thermal analysis (DTA): Mechanism and kinetics assessment, Journal of the Indian Chemical Society, 101 (2024) 101413 https://doi.org/10.1016/j.jics.2024.101413
[58] A. I. A. Ali, M. RASHEED, Effect of changing magnetite percentage on structural and magnetic properties of cobalt ferrite prepared by the sol-gel method, Experimental and Theoretical NANOTECHNOLOGY, 10 (2026) 277 https://doi.org/10.56053/10.s.277
[59] A. Khaleefah, M. RASHEED, Sol–gel-derived mullite nanoparticles: Structural and antibacterial insights, Experimental and Theoretical NANOTECHNOLOGY 10 (2026) 289 https://doi.org/10.56053/10.s.289
[60] Z. S. Ahmed, M. RASHEED, H. S. Ahmed, Optimizing NiO nanoparticle properties for antibacterial applications via temperature-driven structural modification, Experimental and Theoretical NANOTECHNOLOGY 10 (2026) 329 https://doi.org/10.56053/10.s.329
[61] Z. S. Ahmed, M. RASHEED, H. S. Ahmed, Enhancing α-Bi_2O_3 nanoparticle crystallinity and antibacterial functionality through controlled calcination, Experimental and Theoretical NANOTECHNOLOGY 10 (2026) 343 https://doi.org/10.56053/10.s.343
[62] A. I. A. Ali, M. RASHEED, Effect of sintering temperature on electrical and structural properties for spinel ferrites prepared by sol-gel method, Experimental and Theoretical NANOTECHNOLOGY 10 (2026) 239 https://doi.org/10.56053/10.s.239

© 2026 The Authors. Published by LPCMA (https://etnano.com). This article is an open access article distributed under the terms and conditions of the Creative Commons Attribution license (http://creativecommons.org/licenses/by/4.0/).